An improved Bayesian inversion to estimate daily NO_x emissions of Paris from TROPOMI NO_2 observations between 2018-2023

Alba Mols[1], Klaas Folkert Boersma[1,2], Hugo Denier van der Gon[3], and Maarten Krol[1,4]

[1]Wageningen University, Meteorological and Air Quality department, Wageningen, the Netherlands
[2]Royal Netherlands Meteorological Institute (KNMI), De Bilt, the Netherlands
[3]Department of Climate, Air and Sustainability, TNO, Utrecht, the Netherlands
[4]Institute for Marine and Atmospheric Research Utrecht (IMAU), Utrecht University, Utrecht, the Netherlands

Correspondence: Folkert Boersma (folkert.boersma@wur.nl)

Abstract. We present a comprehensive quantification of daily NO_x emissions from Paris using an inverse analysis of tropospheric NO_2 columns measured by the Tropospheric Monitoring Instrument (TROPOMI) over a 5-year period (May 2018 - August 2023). Our analysis leverages a superposition column model that captures the relationship between the increase in NO_2 with distance over an urban source region to underlying NO_x emissions, accounting for chemical transformations and wind in the urban boundary layer. To evaluate the robustness of the superposition column model, we tested it against high-resolution (300 m) Large Eddy Simulations (LES) using MicroHH, a computational fluid dynamics model, with atmospheric chemistry, confirming that the model's simplifying assumptions introduce uncertainties below 10%. Building on this foundation, we develop a new Bayesian inversion method that incorporates prior knowledge on NO_x emissions and lifetimes and accounts for model and prior uncertainties. Compared to a previous look-up table approach, which relied on least-squares minimization without prior constraints, the Bayesian method demonstrated superior performance. In controlled tests, it reproduced known NO_x emissions within 5%. Applying Bayesian inversion to TROPOMI data in Paris, we observed a significant reduction in NO_x emissions from 44 mol s^{-1} in 2018 to 32 mol s^{-1} in 2023, representing a ~~18~~27% decrease. This decline exceeds the 12% reduction predicted by the TNO-MACC-III bottom-up inventory, indicating limited accuracy of current inventories. Seasonal analysis revealed higher posterior emissions in winter, possibly highlighting the role of residential heating or vehicle cold starts, which may be underrepresented in bottom-up estimates. Our improved Bayesian framework delivers accurate NO_x emission estimates that align well with independent data sets. This approach provides a valuable tool for monitoring urban NO_x emissions and assessing the efficacy of air quality policies.

1 Introduction

Nitrogen oxides (NO_x=NO+NO_2) are major air pollutants which are central to the chemistry of the troposphere, and which have negative impacts on human health and the environment (e.g. Boningari and Smirniotis (2016)). In urban regions NO_x is mainly emitted to the atmosphere as a result of the burning of fossil fuels, particularly in combustion engines. In the EU, the largest contributor to NO_x emissions is the transport sector (40%), followed by energy production and distribution (16%), and the commercial, institutional and households sectors (15%) (EEA, 2019). At daytime, nitrogen oxides are short-lived, on the

order of 1-12 hours (Stavrakou et al., 2013), because NO_2 is quickly oxidized by reaction with the hydroxyl radical (OH) to nitric acid (HNO_3)~~, which is deposited by precipitation .~~. Due to its high water solubility, HNO_3 is efficiently removed from the atmosphere, primarily through precipitation and direct deposition onto surfaces (Seinfeld and Pandis, 2016).

Besides being a toxic gas itself, NO_2 also has secondary effects via its contribution to photochemical ozone production (Seinfeld and Pandis, 2016; Jacob, 1999; Visser et al., 2019), its influence on the formation of aerosols (Yan et al., 2020), and its contribution to eutrophication via the deposition of HNO_3 to ecosystems (e.g. Vitousek et al. (1997); Erisman and Draaijers (1995)).

To reduce the negative effects of NO_x, the EU maintains a limit value for average annual surface air NO_2 concentrations of 40 μg m^{-3}. Currently, air quality in most European cities complies (EEA, 2022). Nevertheless, NO_x pollution remains a significant health concern for Europeans, especially in urban areas, as daily guidelines set by the World Health Organisation (WHO) of 25 μg m^{-3} (WHO, 2021) continue to be frequently exceeded (EEA, 2022).

Monitoring of NO_x emissions typically relies on bottom-up inventories, which are uncertain due to their reliance on emission factors, extrapolations and activity assumptions. Uncertainties in bottom-up emissions vary with location, and are estimated to be typically more than 30% (Kuenen et al., 2014). Satellite measurements of NO_2 offer a useful tool for top-down inverse modelling of NO_x emissions, providing more insights into NO_x sources and distributions. However, inverse modelling is also subject to assumptions, such as uncertainties of NO_x lifetimes in the lower atmosphere (Stavrakou et al., 2013), which can significantly influence the accuracy of top-down emission flux estimates.

Research and refinement of inversion methods for estimating NO_x emissions and lifetimes are crucial, especially for initiatives like the Copernicus CO2M mission (Sierk et al., 2021), which will utilize NO_2 plumes to enhance CO_2 monitoring by pinpointing emissions more accurately. Several studies have quantified NO_x emissions based on satellite NO_2 retrievals, by analyzing downwind plumes of NO_2 from large sources, using inverse modeling computations with atmospheric chemical transport models (~~e.g. Brioude et al. (2013); Cheng et al. (2021); Kurokawa et al. (2009); Krol et al. (2024)).~~ CTMs) (e.g. Brioude et al. (2013); Cheng et al. (2021); Kurokawa et al. (2009); Krol et al. (2024); Zhu et al. (2022)). However, because CTMs can have accessibility issues and require substantial computational resources, alternative approaches that do not depend on CTMs have been developed and utilized to estimate NO_x emissions and lifetimes. (e.g. de Foy et al. (2014), Beirle et al. (2011)).

Beirle et al. (2011) first presented a method to infer NO_x emissions from strong isolated sources, by averaging satellite NO_2 plumes with similar wind direction. Building upon this concept, Lorente et al. (2019) presented a simple superposition column model that uses NO_2 retrievals over Paris of the TROPOspheric Monitoring Instrument (TROPOMI), combined with domain-average information about the wind speed, wind direction and OH concentrations in the boundary layer, to estimate urban NO_x emissions and lifetimes without the need for complex inverse modelling computations. This approach allows for day-to-day emission estimates under cloud-free conditions, offering the potential for continuous emission estimations over a long period of time. Zhang et al. (2022) expanded this model framework to estimate the NO_x and ~~predict~~ CO_2 emissions originating from Wuhan, introducing modifications to the method that included considering chemical decay of upwind background NO_2 flowing into the city. Inverse modelling approaches derived from the method of Beirle et al. (2011), as exemplified by

Lorente et al. (2019) and subsequent studies (e.g. Zhang et al. (2022), Goldberg et al. (2022), de Foy and Schauer (2022), Lange et al. (2022), Liu et al. (2022), Rey-Pommier et al. (2022)), inherently simplify the effects of atmospheric dynamics and chemistry. These methods have nonetheless been evaluated using synthetic data, with studies such as de Foy et al. (2014) and Liu et al. (2022) showing that inferred NO_x emissions and lifetimes remain broadly consistent with known model input. In a complementary approach, Zhu et al. (2022) inferred long-term changes in NO_x lifetime from decadal OMI NO_2 columns, using machine learning to relate NO_2 columns urban OH concentrations. Simplifications arise from assumptions that spatially and temporally varying wind speeds, NO_x/NO_2 ratios, and NO_x lifetimes may be taken as constant throughout the inversion domain, whereas in reality there may be substantial temporal and spatial fluctuations in these parameters, especially near the edges of plumes (Hakkarainen et al., 2024; Krol et al., 2024; Meier et al., 2024; Valin et al., 2013; Vilà-Guerau de Arellano et al., 2004). We therefore address the following research questions:

1. To what extent is the forward superposition model capable of simulating realistic NO_2 concentrations, despite simplifications on domain-average wind speed, NO_x/NO_2 ratios, and NO_x lifetimes?

We revisit the methodology introduced by Lorente et al. (2019) and perform an Observing System Simulation Experiment (OSSE). We generate synthetic satellite NO_2 observations using two Large Eddy Simulation (LES) experiments for a hypothetical city to investigate realistic chemical variations that occur in urban plumes. We assess to what extent the simple column model of Lorente et al. (2019) is capable of appropriately capturing NO_2 increases along with the wind over a city despite these simplifications. Next, we move on to the inversion of NO_x emissions, and pose the question:

2. Can a Bayesian inversion method that weighs prior information, forward model uncertainty, and observational uncertainties improve estimates of NO_x emissions from TROPOMI NO_2 plumes relative to a method that does not account for constraints imposed by prior knowledge?

We propose and evaluate a new more formal Bayesian inversion method, incorporating prior knowledge on NO_x emissions and NO_x lifetime and observations of NO_2 and their uncertainties. In Sections 2 and 3, we use the synthetic observations sampled from simulations with a high-resolution computational fluid dynamics model that resolves large-scale turbulence and atmospheric chemistry (MicroHH (Van Heerwaarden et al., 2017)) to evaluate the forward superposition model and inferred emissions. Then in Section 4, to demonstrate the applicability of this method, we infer a 5-year timeseries of NO_x emissions for Paris on individual clear-sky days between June 2018 - August 2023 using improved TROPOMI NO_2 V2.4.0 retrievals. This retrieval product is based on high-resolution (0.125°) surface albedo information from the DLER database (Tilstra et al., 2023) and high-resolution (0.1°) a priori NO_2 profiles from CAMS (Douros et al., 2022). TROPOMI NO_2 retrievals based on high-resolution input data have been shown to capture NO_2 gradients well (Lange et al., 2024). The inversion illustrates the potential of the method and allows us to identify trends and patterns in the NO_x emissions of Paris, including seasonal and weekly emission cycles, and to assess the effectiveness of pollution reduction efforts. We conclude with an evaluation of our top-down NO_x estimates with an independent bottom-up inventory of NO_x emissions of Paris.

2 Forward superposition column model

2.1 Model setup

The superposition column model first presented by Lorente et al. (2019) calculates NO_2 columns by superimposing NO_x emissions along the wind within a region. The region (e.g. a city) that is analysed is divided into line cells that encapsulate the entire source region perpendicular to the wind direction (Fig. 1, (Beirle et al., 2011)). For each cell i between, within, and beyond the city length, the contribution to the NO_2 line density downwind to the cell is calculated using a simple column model:

$$
\begin{aligned}
f_i(x) &= 0 && \text{for } x < x_i \\
f_i(x) &= \frac{E_i}{k}(1 - e^{-k(x-x_i)/u}) \times \frac{[NO_2]}{[NO_x]} && \text{for } x = x_i \\
f_i(x) &= \frac{E_i}{k}(1 - e^{-kL/u}) \times e^{-k(x-x_i)/u} \times \frac{[NO_2]}{[NO_x]} && \text{for } x > x_i
\end{aligned}
\tag{1}
$$

Where f_i is the contribution of the emissions in cell i to the NO_2 line density at x (mol cm^{-1}), $E(x_i)$ represents the NO_x emissions from cell x_i (mol cm^{-1} s^{-1}), L is the length of each line cell (m) and u is the effective wind speed at which NO_x is transported (m s^{-1}). This effective wind speed is determined by weighing the vertical wind speed profile by the the vertical NO_2 density profile, as described in Lorente et al. (2019). The scaling with the $[NO_2]/[NO_x]$ ratio is required because a fraction of NO_x is present as NO_2, and TROPOMI measures the NO_2 columns. k is the rate constant of the chemical loss of NO_x during daytime (s^{-1}): $k = \frac{k'[OH]}{[NOx]/[NO2]}$, using the reaction rate constant k' of $1.1 \cdot 10^{-11}$ cm^3 $molecule^{-1}$ s^{-1} for the OH + NO_2 + M reaction at surface pressure for ~~298K (Burkholder et al., 2020).~~ 288K (Burkholder et al., 2020). PAN formation is not explicitly considered in this framework, as it is a reversible NO_x reservoir rather than a permanent sink:(e.g., (Fischer et al., 2014)). In the warm, VOC-limited conditions typical of central Paris (e.g., Johnson et al. (2024)), PAN decomposes rapidly and contributes little to net NO_x loss. The dominant NO_2 sink under these conditions is oxidation to HNO_3.

The contributions to the line density from each cell are added to the background NO_2 concentration (b) to find the overall NO_2 line density at each distance x along with the wind:

$$
F(x) = \sum_{i=1}^{n} f_i(x) + b \tag{2}
$$

Following this model formulation, the NO_2 that accumulates over the city $F(x)$ depends on ~~on~~ the spatial pattern of emissions $E(x)$ within the city and is affected by the chemical loss and the wind speed over the city, as discussed extensively in the studies by Lorente et al. (2019) and Zhang et al. (2022). The superposition column model defined by Eqs. (1) and (2) implies that prior knowledge is required on oxidation chemistry (OH concentration and NO_x:NO_2 ratio) within the urban boundary layer, and that the background b represents the spatially invariant free tropospheric NO_2 contribution to the line density.

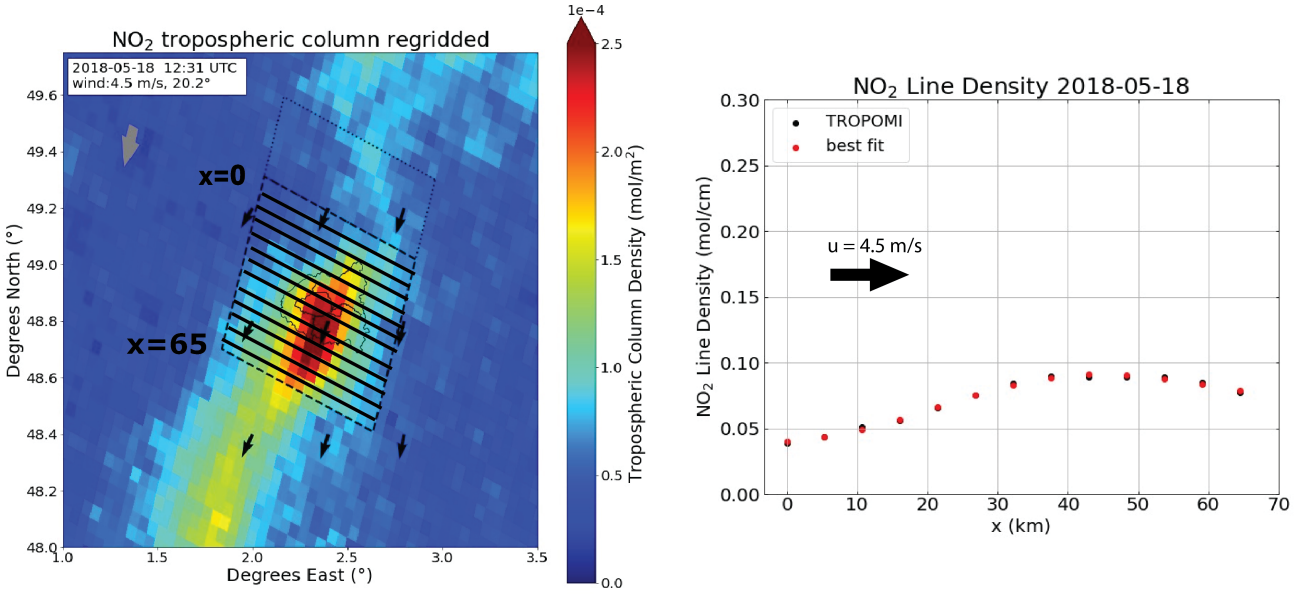

Figure 1. Left: the study area of wider Paris and illustration of the line density method. The black solid lines indicate the different line cells. The ~~grey arrow indicates~~ black arrows indicate the ~~mean~~ wind speed (from the ~~northeast~~north-east). The dotted grey box to the north of Paris represents the background area. Right: NO_2 line densities at each distance x, calculated from the TROPOMI retrieval on 18 May 2018.

2.2 Comparison superposition model to synthetic NO_2 satellite observations with MicroHH

To generate synthetic satellite observations of NO_2, we use MicroHH, a direct numerical simulation (DNS) and large-eddy simulation (LES) model (Van Heerwaarden et al., 2017), which has recently been extended to include an atmospheric chemistry module based on the Kinetic Pre-Processor package (KPP) (Krol et al., 2024). We set up a horizontal model domain of 50 km (North-South) × 150 km (East-West) × 4 km (vertical), with a horizontal resolution of 300 m and a vertical resolution of 100 m. At the upper end of the model domain, a buffer zone of 750 m serves to damp gravity waves (Van Heerwaarden et al., 2017). For temperature, humidity, and momentum, circular boundary conditions were used. To avoid re-entering of emissions from the city source, we employed free outflow conditions for tracers (Ražnjević et al., 2022). More information about the MicroHH setup and initial conditions used can be found in section 1 of the Supplementary Material.

We conduct two MicroHH simulations over a hypothetical city ('symcity') to assess the capability of the forward line density model (Eq. 1,2) to realistically simulate line densities over a city, despite its simplifications (a spatio-temporally constant windspeed, NO_x:NO_2 ratio, and NO_x-lifetime). Our simulated city, 30 km × 30 km in size, is positioned on the west side of the model domain, which is dominated by a westerly flow. NO_x is emitted within the city as NO, and gradually transformed to NO_2 by reaction with ozone. The NO emissions are spatially distributed over the city in a Gaussian pattern, so that the emissions are much larger in the center. 68% of the emissions lie within a radius of 7.5 km around the city center, and 95% within 15 km. The

simulation is performed between 6:00 and 18:00 hrs local time. Photolysis representative for the city of ~~Riaydh~~ Riyadh is used in the simulation. We simulate two different scenario's: scenario 1 is a Spring case (photolysis of April 15th) which has high NO emissions of 195.7 mol s^{-1}, and a high wind speed of 6 m s^{-1}. Scenario 2 is a winter case (photolysis of December 15th) and has lower NO emissions of 58.7 mol s^{-1} and a wind speed of 2 m s^{-1}. Details of the two cases are summarized in Table 1. Figure 2 displays the MicroHH tropospheric NO_2 columns between 0-4 km height at 13:00 hrs, close to the approximate TROPOMI overpass time of 13:30 hrs. Since the emissions are smoothly distributed over the city, the irregularities in the simulated NO_2 columns, visible in the upper panels, are caused by the combined effects of atmospheric turbulence and chemistry. The lower panel shows the columns averaged to a ~~5~~ 3 km × ~~5~~ 3 km resolution, more similar to the spatial resolution of the TROPOMI NO_2 retrievals.

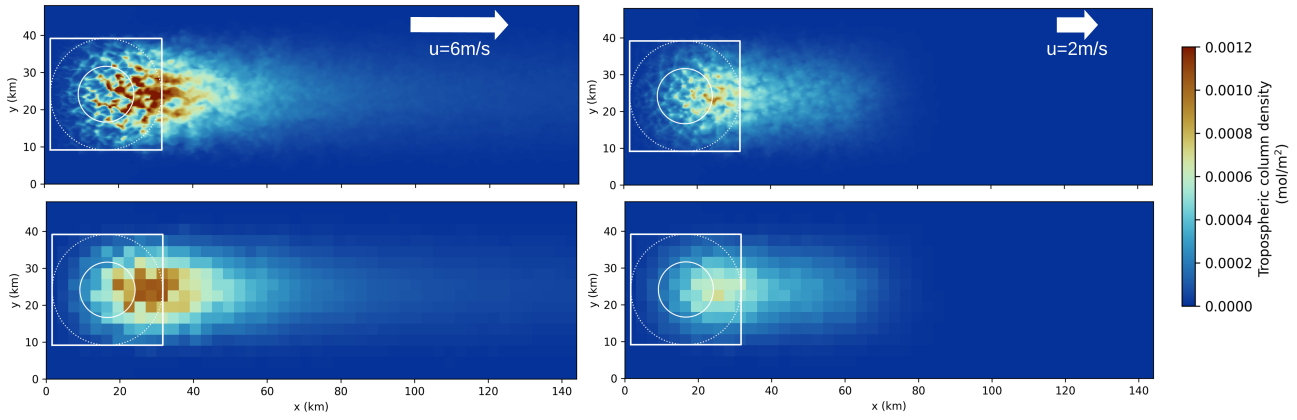

(a) Case 1: high emissions , high wind speed

(b) Case 2: low emissions , low wind speed

Figure 2. Tropospheric NO_2 columns of symcity simulated by MicroHH for a Spring atmosphere with high NO_x emissions and strong wind (left panels), and a Winter atmosphere with low NO_x emissions and weak wind (right panels). 68% of the NO_x emissions occur within the smallest circle, and 95% within the bigger circle. The upper panels show the NO_2 columns at the MicroHH spatial resolution of 300 m, and the lower panels show the same MicroHH simulations regridded to ~~5~~ 3 km resolution.

Building upon the ~~5~~ 3 km × ~~5~~ 3 km resampled simulations, we computed NO_2 line densities across symcity, depicted as black dots in Fig. 3c and 3f. The simulated NO_2 line densities over the city exhibit a tilted S-shaped pattern, similar as the observed line densities over Paris reported in Lorente et al. (2019). This pattern is a consequence of the dynamic interplay between wind and the Gaussian emission distribution across the city, with maximal emissions concentrated at the city center. NO_2 columns are very low upwind of the city, and the NO_2 line densities increase once the emitted NO is converted into NO_2 via the $NO+O_3$ reaction in the boundary layer. For the Spring case, with 6 m s^{-1} wind speed, the NO_2 line density peaks downwind of the city, reflecting the rapid transport of NO_2 beyond the city limits. The Winter case shows the NO_2 line density peaks over the city, at about 25 km, reflecting the lower wind speed in that simulation.

We evaluate the forward superposition model (based on Eq. (1) and Eq. (2)) by comparison to line densities we directly obtained from MicroHH. For the forward model, we use the NO_x emissions (magnitude and spatial distribution) and other model input parameters (the average NO_x lifetime, wind speed, and the average NO_x/NO_2 ratio (Eq. 1)) from the symcity test (these average values are listed in Table 1). We try to determine these parameters as closely as possible to data we would obtain from CAMS (Copernicus Atmosphere Monitoring Service), to ensure a realistic representation of conditions encountered in a TROPOMI inversion scenario (Lorente et al., 2019). The high resolution of the MicroHH model enables us to discern the implications of these simplifications. We calculate the parameter values from the MicroHH output of 12:00 hrs local time, as the observed NO_2 columns ~~observed~~ depend on the conditions of preceding time steps. In the MicroHH simulation, the NO_x lifetime ranges between 1-6 hours (2-9 h for case 2) within the city domain (Fig. 3a,d). The NO_x lifetime is especially short in the downwind part of the plume, reflecting high OH concentrations in the urban plume (there were also substantial hydrocarbon emissions from the city, which leads to O_3 formation and consequently enhanced OH). The NO_x/NO_2 ratio ranges between 1.2-1.7 (1.2-1.6 for case 2) over the city domain (Fig. 3b,e). For the Winter case (case 2) O_3 and OH concentrations are slightly lower than for the Spring case (case 1). This leads to a slightly longer NO_x lifetime, and a lower NO_x/NO_2 ratio than for the Spring case. In the MicroHH simulations, the wind speed remains relatively constant across the entire domain. The domain average wind speed, weighted vertically by the vertical NO_2 concentration is around 6 m/s for Spring and 2 m/s for Winter.

Our superposition model requires effective values of wind, NO_x/NO_2 and NO_x lifetime as input parameters. Simulating NO_2 line densities over the city using the superposition model with the domain averaged input parameters from MicroHH yields the values shown as red dots in Fig. 3c,f. We see that despite simplifications, the simulated line densities from the superpopsition model closely match those from the MicroHH simulation. The agreement between the superposition and MicroHH NO_2 line densities allows us to estimate the superposition forward model error. We estimated the forward model error as the average absolute deviation for the 10 line density values along with the wind~~, and~~ . It amounts to 6.5% from the average MicroHH line density for case 1 and 6.3% for case 2. This suggests that, despite simplifications, the superposition model is effective and provides realistic NO_2 line densities based on city-domain averaged NO_x emissions, lifetime and NO_x/NO_2 ratio and wind speeds, at least at the spatial resolution of TROPOMI NO_2 observations.

Table 1. The range of parameter values within the city domain for the two cases of the MicroHH simulations for a Riyadh-like city, at 13:00, and the domain-averaged parameters used in the forward model simulations. The wind speed used in the forward model is the height-averaged wind speed weighted by the vertical NO_2 distribution. The range displayed for MicroHH is the city-domain averaged wind speed at 100 m height and 3 km height.

	Photolysis		Total E_{NO_x} ~~Total E_{NO_x}~~ (mol s^{-1})	Wind speed (ms^{-1})	NO_x lifetime (h)	NO_x/NO_2 ratio	Line densities
Case 1	15 Apr	MicroHH	195.7	4 (100 m) - 8 (3 km)	~~1.6~~ 2.6±1.2 ~~1.7~~	1.5±0.08	Black dots in Fi
		Forward model		5.7	2.21	1.48	Red dots in Fig.
Case 2	15 Dec	MicroHH	58.7	2 (100 m) - 3 (3 km)	~~2.9~~ 3.4±1.8	~~1.2-1.6~~ 1.4±0.08	Black dots in Fi
		Forward model		2.3	2.87	1.4	Red dots in Fig.

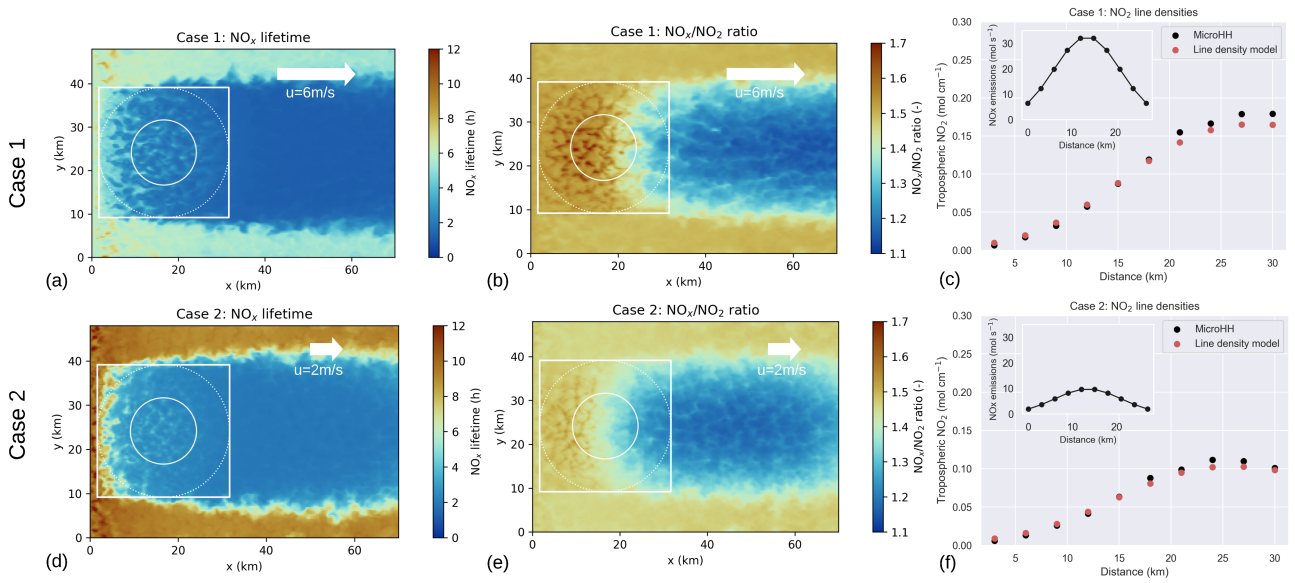

Figure 3. NO_x lifetimes and NO_x/NO_2 ratios for the two cases as simulated by MicroHH over the entire domain. Simulated line densities over ~~simcity~~ symcity of MicroHH and the line density model (c,f). The emission profile over the city is displayed in the small panel. The city-domain averaged conditions are given in the white box. Figures are for 13:00 hrs local time.

3 Inversion of NO_x emissions and lifetime

We now assess the ability of the inverse superposition model to estimate known input NO_x emissions and lifetimes based on the NO_2 line densities as simulated by MicroHH, again using the two MicroHH simulations regridded to a TROPOMI resolution.

3.1 Inversion methods

Since TROPOMI measures NO_2 columns, we need to estimate the NO_x emissions using auxiliary and a priori knowledge of wind, chemical regime and emissions. In Lorente et al. (2019) a simple inversion method is used for this: the forward model (Eq. 1, 2) is fitted to the observed NO_2 line densities by minimizing the sum of the squares of the residuals, using a pre-calculated look-up table with a large number of NO_2 line densities corresponding to combinations of NO_x emissions and NO_x lifetimes, which are allowed to vary by $\pm 50\%$ from their prior values. No formal weight is assigned to prior knowledge regarding NO_x emissions and lifetimes. The optimal solution is determined by the NO_x emissions and lifetimes that result in the lowest residuals between observed and pre-calculated line densies. The optimal solution (with the lowest residuals) according to the procedure in Lorente et al. (2019) may therefore include some estimates of NO_x emissions and lifetimes that are unrealistic, e.g. with large emissions accompanied by large OH.

Here we propose a new, more formal inversion method that uses the minimization of the Bayesian cost function, taking into account knowledge on uncertainties of the prior emissions and lifetime, uncertainties in the forward model (see section 2.2), and uncertainties in the measured line densities:

$$J(x) = \frac{(x - x_a)^2}{\sigma_A^2} + \frac{(F(x) - y)^2}{\sigma_O^2} \tag{3}$$

Where x is the state vector, including all the terms that are fitted (k, and the emissions from each line cell). The cost function is minimized by finding the solution of $dJ/dx = 0$. The cost function comprises two different terms. The first term is the deviation of the prior estimate (x_a) of the state from the actual state (x). The second term is the deviation of the calculated line densities ($F(x)$) from the measured line densities (y), given the solution for the state x. Both terms are weighted by their uncertainties. σ_A represents the uncertainty in the prior, and σ_O represents the combined measurement uncertainty and the uncertainty in the model representation of the system. With this Bayesian inversion method, we take into account not just the observations but also our prior knowledge. This prevents the model from excessively conforming to the observed data ("overfitting"), which is problematic in the basic inversion method. The main differences between the least-squares inversion method from Lorente et al. (2019) and the Bayesian inversion approach are displayed in Table 2.

Table 2. Differences between the least-squares and the Bayesian inversion method in inferring the NO_x emissions and lifetimes from the NO_2 line densities.

	(1) least-squares inversion	(2) Bayesian inversion
Cost function	$J(x) = (F(x) - y)^2$ (4)	$J(x) = \frac{(x - x_a)^2}{\sigma_A^2} + \frac{(F(x) - y)^2}{\sigma_O^2}$ (5)
Condition state parameters	~~k~~ $\tau \pm 0.5$~~k~~ τ $E \pm \infty$	~~k~~ $\tau \pm$ ~~$\sigma_{A,k}$~~ $\sigma_{A,\tau}$ $E \pm \sigma_{A,E}$

3.2 Symcity emission inversion

We now apply the two inversion methods to infer the NO_x emissions and lifetimes of symcity based on the NO_2 columns from MicroHH, for both the high and low emission scenario. First, we assume zero observational error, and only uncertainty in the model representation of the system. We use a σ_O of 6%, representing the model representation uncertainty that we determined in section 2.2. We use a prior lifetime uncertainty ~~$\sigma_{a,k}$~~ $\sigma_{a,\tau}$ of 30%, and a prior emission uncertainty $\sigma_{a,E}$ of 50%. First, we assume known prior conditions, so the emission profiles over the city and city-average lifetimes from MicroHH are used as the prior for the Bayesian model. The results of the inversions are presented in Table 3. The Bayesian inversion method yields emissions that closely match those input into MicroHH (within 2%). The least-squares inversion method slightly underestimates emissions (4%) and overestimates lifetimes for case 1, and vice versa for case 2 (16% emission overestimation)

highlighting overfitting issues inherent in the least-squares inversion approach. Although the Root Mean Square Error (RMSE) is smaller when using the least-squares inversion method, there are slight discrepancies in the inferred emissions and lifetimes due to this overfitting.

Table 3. Comparison of $E_{NO_x,tot}$, τ_{NO_x}, and RMSE values for different inversion methods: MicroHH, least-squares inversion, and Bayesian inversion.

	Case 1			Case 2		
	$E_{NO_x,tot}$ (mol s^{-1})	τ_{NO_x} (h)	RMSE (mol s^{-1})	$E_{NO_x,tot}$ (mol s^{-1})	τ_{NO_x} (h)	RMSE (mol s^{-1})
MicroHH	195.7	2.21		58.7	2.87	
Least-squares inversion	188	3.31	0.002	69.9	2.26	0.0016
Bayesian inversion	196.7	2.77	0.003	57.9	3.09	0.0021

This first inversion was performed for the idealized scenario, with zero observational uncertainty. To enhance the similarity of the NO_2 columns in MicroHH to what TROPOMI would observe, we introduced uncertainty on top of the MicroHH-simulated NO_2 columns. We prescribe this uncertainty as:

$$\sigma = 0.4 \cdot 10^{15} + 0.2 \cdot N_v \ \ (\text{molecules cm}^{-2}) \tag{6}$$

Where N_v is the NO_2 column. The first part represents random uncertainty in TROPOMI measurements (originating from measurement noise in the satellite level-1 data), while the second part accounts for systematic uncertainty in estimating the Air Mass Factor (AMF), for instance caused by to uncertainties in albedo estimates (Van Geffen et al., 2022; Riess et al., 2023). ~~This uncertainty is partially~~ The systematic part is correlated between adjacent cells~~(e.g. Rijsdijk et al. (2024)~~, with a Gaussian-like shape between adjacent cells with a spatial correlation length (where the correlation falls to 1/e) of 7km (e.g. Rijsdijk et al. (2025)). We perform 1000 inversions with different random uncertainty, drawing them from a normal distribution with the standard deviation defined in Eq. 6.

The results are displayed in Fig. 4. Here we show the mean emission estimates for all 1000 runs with uncertainty on the NO_2 columns, for the true MicroHH emissions, the prior estimate, the Bayesian emission inversion and the Least-squares inversion. We do this for both case 1, the Spring case with high emissions (Fig. 4a) and case 2, the Winter case with lower emissions (Fig. 4b). In this more realistic setup, which uses realistic TROPOMI uncertainties instead of the idealized inversion of Table 3, emissions are more frequently overestimated in both MicroHH cases when using the least-squares inversion method than when using the Bayesian method.

We also investigate the extent to which NO_x emissions and lifetime can be independently and simultaneously reproduced. Figure 4~~e~~b,d shows the correlation between the errors in the inferred lifetime and emissions. The observed errors in the inferred NO_x emissions and lifetimes exhibit substantial correlation. An overestimation in emissions is consistently accompanied by an underestimation in lifetime and vice versa. This relationship is in line with the fundamental equation of the superposition column model (Eq. 2), where both elevated emissions and extended lifetimes contribute to increased line density values. These

inversions of the emissions from MicroHH provide evidence and quantitative insights into the strength of this correlation. The figures demonstrate a nonlinear relationship between the errors in inferred NO_x emissions and lifetimes, where the cross-correlation appears strongest when the lifetime is underestimated. This points to a logarithmic cross-correlation between the error in NO_x lifetimes and emissions, suggesting that small deviations in lifetime have a more substantial impact on emissions when the lifetime is underestimated.

The deviations in the inferred emissions are generally larger for the least-squares inversion method. Figures 4b,d clearly show that the lifetimes tend to be estimated at either the -50% or +50% limit that is restricted in the fit. Because of this, the emissions are also estimated in two modes, where one is close to the true value and in the other case, emissions are overestimated. For the Bayesian model, the fit is kept in check by the prior estimate, preventing overfitting, and leading more often to the right emission estimate. For the Bayesian inversion, the median error in the emission estimate of case 1 (case 2 in brackets) is -0.7% (-5.1%) and the standard deviation is 6.9% (11.3%). For the least-squares inversion, the median is 14% (26%) and the standard deviation is 22% (34%). Regarding the lifetime, the median error in the lifetime estimate of case 1 (case 2 in brackets) is 32% (13%) for the Bayesian inversion and the standard deviation is 31% (61%). For the least-squares inversion, the median is 2% (-19%) and the standard deviation is 46% (37%). To investigate the sensitivity of our results to deviations in the prior, we conducted an additional test. We repeated the OSSEs for both Symcity cases 50 times, introducing a $\pm$20% deviation in either the prior lifetime or emissions. These sensitivity tests show that increasing or decreasing the prior emissions by 20% results in a posterior bias of no more than 6% compared to the case with a known prior. Detailed results can be found in section 2 of the Supplementary Material.

We showed here that the strong correlation between errors in estimated NO_x emissions and lifetimes makes their independent estimation difficult. The Bayesian inversion outperforms the least-squares method in estimating NO_x emissions with more accurate and consistent results while avoiding the bimodal errors of the least-squares approach. Lifetimes, however, remain more challenging to reproduce and show mixed results between the two methods. The sensitivity tests show that also with deviating prior information, the Bayesian inversion method outperforms the Least-Squares approach, producing smaller biases and a smaller standard deviation.

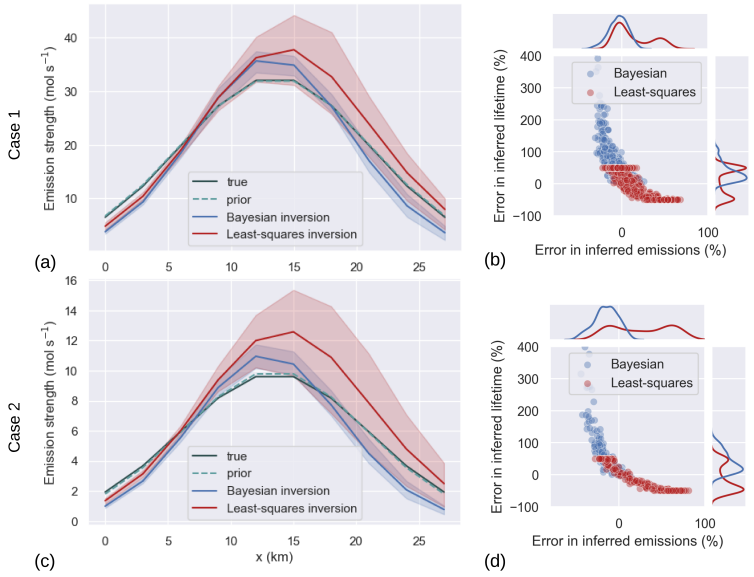

Figure 4. a,c) Mean emission strength of each 5 km line cell along the city for an ensemble of 1000 randomly generated noise profiles over the city for both cases. The shaded areas indicate the interquartile range. b,d) The correlation between the deviation from the true NO_x emissions and lifetimes, with kde (kernel density estimate) plots in the margins. For the Bayesian inversion (blue) and the least-squares inversion (red).

4 Model application: NO_x emission estimations Paris

We now apply the two inversion methods of the superposition column model (the least-squares method and the Bayesian method) to daily clear-sky TROPOMI NO_2 data to estimate NO_x emissions of Paris between June 2018 - July 2023 at the TROPOMI overpass time of around 13:00 local time. We use the ~~improved TROPOMI V2.4.0 data product , which~~ European TROPOMI NO_2 product that uses CAMS a priori NO_2 profiles in the air mass factor and averaging kernel calculation~~(Douros et al., 2022). ~~. This product is based on the operational TROPOMI NO_2 (v2.4.0) version, and is described in Douros et al. (2022). We do not apply averaging kernels (Eskes and Boersma, 2003), because the superposition column model does not provide tropospheric NO_2 profiles. ~~Comparisons with independent NO_2 data revealed an improvement in the overall bias of~~ The standard and European NO_2 product has been compared with ground-based remote sensing measurements of nine Multi-AXis Differential Optical Absorption Spectroscopy (MAX-DOAS) instruments by Douros et al. (2022). They found an average bias over all stations of the standard TROPOMI version of -31%. For the European product, this bias is -19%. As compared to the standard S5P tropospheric NO_2 ~~when using this TROPOMI product~~ column data, the overall bias of the European product for almost all stations is 5 % to 18% smaller, with NO_2 columns up to 30% higher than previous in emission hotspots, especially in Winter (Douros et al., 2022)~~, providing~~ . This provides good confidence in using TROPOMI tropospheric NO_2 columns from the European product for the purpose of estimating NO_x emissions.

4.1 ~~Inferring NO_x emissions from TROPOMI NO_2 columns~~

4.0.1 ~~Computation TROPOMI line densities~~

~~The TROPOMI data are first re-gridded and rotated in the wind direction.~~ A quality check is applied where less than 10% of the TROPOMI pixels in the study area are allowed to be below a quality assurance (QA) value of 0.75 (recommended by van Geffen et al. (2022)). In this way, cloudy days or problematic retrievals are filtered out.

4.1 Inferring NO_x emissions from TROPOMI NO_2 columns

4.1.1 Computation of TROPOMI line densities

For the calculation of the line densities, the TROPOMI NO_2 data is first rotated towards the effective wind direction (elaborated in the next section) and re-scaled into grid cells of $0.05 \times 0.05°$. Specifically, we do this by generating a target grid with a $0.05° \times 0.05°$ resolution, aligned parallel to the wind direction at the time of the TROPOMI overpass. The TROPOMI NO_2 data are then regridded onto this new grid, using weights based on the overlapping areas between the original and target grids.

Within the 65×65 km study domain, the grid cells are divided into 13 'line cells' along the wind direction, as illustrated in Fig. 1 for the TROPOMI overpass on 18 May 2018. Subsequently, the line densities are calculated by accumulating all the pixels within each line cell, and dividing by the total width. The result is one value of the NO_2 line density for each 'line cell', with units of mol/cm. This is a transformation of a 2-D (65×65 km^2) field into a 1-D line density, which simplifies the analysis, at the cost of giving up any constraints on the across-wind emission distribution.

The result of this line density transformation is shown for the overpass on 18 May 2018 in the right panel of Fig. 1. Here, the line densities are shown for each distance, where $x = 0$ is the upwind start of the area. In the case of this example, the line densities are increasing until 40 km, followed by a slight decay. This pattern arises from higher emissions in the center of Paris, at $x \sim 30$ km, after which emissions are lower and decay of NO_2 dominates (Lorente et al., 2019).

4.1.2 Estimating NO_x emissions and lifetimes

To compute the NO_x lifetimes and emissions across the city, the superpositon model (Eq. 1) is fitted to the calculated TROPOMI NO_2 line densities using the two different inversion methods: the least-squares method and the Bayesian variant.

The background NO_2 level (b) is defined as the average line density value in a box of 30 km upwind of the study area (light grey dotted box in Fig. 1). In this definition, chemical loss of background NO_2 by reaction with OH is neglected, because the background NO_2 is assumed to be mostly located above the boundary layer where OH concentrations are assumed to be lower than in the photochemically active boundary layer. The domain average, boundary layer mean NO_x/NO_2 ratio over Paris is taken from CAMS ($0.4° \times 0.4°$resolution), 1h before the TROPOMI overpass time. The CAMS 0.4°forecast product is part of the Copernicus Atmosphere Monitoring Service and provides global 5-day forecasts of atmospheric composition at approximately 0.4°(40 km) resolution. Similarly, we take CAMS boundary layer mean OH as prior in our Bayesian inversion. Using CAMS

OH as a prior is justified by its physical consistency, full spatiotemporal coverage, and compatibility with the scale of the rotated line densities and column model, which assumes a single effective NO_x lifetime. The domain and boundary layer average wind speed, weighted by the vertical NO_2 concentration from CAMS, is taken for 1h before the TROPOMI overpass from ERA5, the fifth-generation ECMWF (European Centre for MediumRange Weather Forecasts) atmospheric reanalysis of the global climate.

4.1.3 Prior estimates and uncertainties

The TNO-MACC-III NO_x emission inventory of 2011 (Kuenen et al., 2014) is used as a prior estimate of the NO_x emissions over Paris. This inventory predicts a total prior NO_x emission of 52.8 mol s^{-1} over Paris for 2011. We scale this value of 2011 to the years 2018-2023 using predicted NO_x emission reductions after 2011 of France by the EEA ranging from -27% for 2018 to -49% for 2023 (EEA, 2023). In 2020 and 2021, France took measures to prevent the spread of the coronavirus outbreak (Covid-19), which caused reductions in industrial activities and traffic intensity. To correct for this decrease in activity, we account for an additional decrease in the prior emissions of 40% during the three Covid-19 lockdown periods of France (Guevara et al., 2021; Ikhlasse et al., 2021). The NO_2 concentrations in Paris never completely ~~decreased to their original levels inbetween~~ increased to their pre-Covid levels in between the lockdown periods (Pazmiño et al., 2021), which is why we assume that prior emissions were reduced by 20% in between the lockdown periods. A timeseries of these prior NO_x emissions is displayed in the light green line of the upper panel of Fig. 5.

For a more realistic prior value than one yearly average, we scale the emissions using monthly, weekly and hourly emission factors from TNO (Denier van der Gon et al., 2011), based on prior knowledge of human activities. These factors are given per source sector. We weigh the temporal emission factors by the contribution of the source sectors of Paris according to the European Union (EU, 2019). This gives us an hourly scaling factor of 1.17 for 12:00 (around the TROPOMI overpass time), because of higher traffic intensity at 12:00 relative to the 24-hour mean values. We also apply additional scaling factors varying per month and weekday. These are higher for Winter months, when there is more residential heating, and vehicles suffer more from so-called cold starts (Tu et al., 2021) and lower for weekend days because of reduced traffic intensity. A timeseries of this corrected prior NO_x emission, including the scaling factors, is displayed in the dark green line of the upper panel of Fig. 5. It should be noted that our constructed prior is intentionally simple and straightforward. The prior only needs to be a good starting point, but the observations will adjust the posterior emissions towards the most accurate solution.

For the prior estimate of the NO_x lifetime, the domain-average, boundary layer mean hydroxyl radical (OH) concentration is taken from CAMS for one hour before the TROPOMI overpass.

In the Bayesian inversion method, NO_x emissions and lifetimes are permitted to deviate from the prior, constrained by observation and prior uncertainties. We use a line density observation uncertainty σ_o of 10%, accounting for both the measurement uncertainty and the uncertainty of the model representation of the system. To incorporate the uncertainty in OH concentrations and its impact on the NO_x lifetimes, we choose a standard deviation of 30% on the prior lifetime ($\sigma_{A,k}$ $\sigma_{A,\tau}$). This selection aligns with the typical range of uncertainty observed in NO_x lifetimes, which commonly falls within 50% (Lorente et al., 2019). By adopting a standard deviation of 30%, we encompass the majority of uncertainties within the expected 50% range, while

also allowing for larger deviations in exceptional cases. Finally, to account for uncertainty in the TNO-MACC-III inventory, we assign a standard deviation of the prior emissions ($\sigma_{A,E}$) of 30% in each individual point (Kuenen et al., 2014)).

4.2 NO_x emission estimations Paris

4.2.1 Emission estimates 2018-2023

For the period spanning May 2018 to July 2023, we obtained 752 TROPOMI NO_2 retrievals over Paris that are under predominantly clear-sky conditions and of sufficient quality to perform NO_x emission estimates. Some of these estimates are in duplicate because Paris is observed from two subsequent satellite overpasses on some days. This results in 560 inversions corresponding to unique days. Initially, the emission inversions were conducted with both the Bayesian method and the method outlined by Lorente et al. (2019). The time-averaged estimates of both methods were similar, but the latter revealed substantial outliers in NO_x emission estimates, reaching up to 250 mol s^{-1} on some days, and lifetimes were underestimated, particularly on days with low wind speed. This underscores the overfitting issue that we raised in the previous section. We therefore continue analysing the NO_x emission estimates from the Bayesian inversion. Table 4 shows the average conditions across all inversions.

Table 4. Average meteorological and chemical conditions over Paris throughout the period May 2018 - July 2023, and prior and posterior NO_x emissions and lifetimes during the TROPOMI overpass time (around 12:00). NO_x/NO_2 ratios and wind speeds are derived from CAMS, and temperatures are measurements from the Montsouris weather station in Paris. Averages are given for the whole period and for the Summer and Winter months separately, the range is one standard deviation.The posterior standard deviation is estimated through a Monte Carlo analysis, using ~~100~~ 50 randomly drawn prior and observation values, with their prescribed uncertainties as standard deviations, for ~~one specific day (16/06/2023).~~ eight distributed days in 2022.

					NO_x lifetime (h)		NO_x emissions (mol s^{-1})	
	n	NO_x/NO_2	Wind speed (m s^{-1})	Temperature (°C)	Prior	Posterior	Prior	Posterior
Year-round	752	1.40 ± 0.12	4.6 ± 2.3	20.4 ± 8.1	5.2 ± 30%	6.0 ± ~~14~~3.9%	35 ± 30%	32 ± ~~10~~6.1%
Winter (DJF)	114	1.53 ± 0.19	5.4 ± 2.8	9.5 ± 4.4	30	27	39	40
Summer (JJA)	243	1.33 ± 0.09	4.0 ± 1.9	28.4 ± 3.8	2.7	2.3	31	28

The CAMS-derived domain average NO_x/NO_2 ratios, averaging to 1.4 over all inversions, exceeded the commonly adopted ratio of 1.32. This discrepancy results in higher NO_x emission estimates than if the constant value of 1.32 would be used. Daily temperatures, recorded at 13:00 from the Montsouris weather station in Paris city center, consistently appear relatively high, potentially influenced by urban heat island effects and our clear-sky sampling. Our findings indicate slightly lower average NO_x emissions than the prior estimates, especially during the Summer months. We find an average top-down NO_x emission over Paris of 32 mol s^{-1}, which is slightly lower than the prior (9% year round), especially during the Summer months (11%).

The ~~lower panel~~ middle panel (b) of Fig. 5 displays the monthly average NO_x emissions of Paris estimated with the Bayesian inversion method (blue line). Values from the CAMS-REGv7 inventory are displayed in red. This is an improved version of the v4 dataset described by Kuenen et al. (2022). We scale these values using emission factors from Guevara et al. (2020, 2021)

Figure 5. Upper panel: NO_x emissions from the TNO-MACC III emission inventory, corrected for the emission reductions predicted by the EEA, and for emission reductions during COVID (light green). The dark green line shows daily predictions, accounting for the weekly and monthly cycle and uses a scaling factor of 1.17 (relative to the 24-hour mean) for the TROPOMI overpass time. Lower ~~panel~~two panels: monthly median values of the prior (green) and posterior (blue) NO_x emission (b) and lifetime (c) estimates. The prior is resampled to the days with TROPOMI NO_2 retrievals. The errorbars represent the interquartile range within each month.

(more information about how we calculated these values can be found in section ~~2~~ 3 of the Supplementary Material). To ensure a fair comparison, the prior estimate in this graph is resampled on days with valid inversions, resulting in a slight variation from the upper panel. The monthly average posterior NO_x emissions exhibit more variability than the prior~~, indicating~~. Higher variability of posterior emissions is expected because of uncertainties in their derivation. Additionally, posterior emissions reflect real day-to-day and diurnal fluctuations, while prior emissions are based on climatological averages and are therefore inherently less variable. This difference between prior and posterior NO_x emissions indicates that factors beyond the month and day of the week influence ~~NO_x~~ the emissions.

We observe an overall decreasing trend from 44 to 32 mol s^{-1} (~~17.5~~27%) in NO_x emissions between May 2018/19 and August 2022/23. This decreasing trend can be partly attributed to the Paris low-emission zone, which was estimated to reduce traffic NO_x emissions by about 20% between 2018-2023 due to the adoption of cleaner vehicles (Bernard et al., 2020). Significantly lower NO_x emissions are visible during the Covid-19 lockdown periods, even lower than our prior assumptions. Especially during the first Covid-19 lockdown (17/03/2020-11/05/2020) the NO_x emissions dropped substantially. We quantified the effect of the Covid-19 lockdowns by calculating the change in emissions between the lockdown periods in 2020-2021 and the prior of the same periods in 2019. We find a significant decrease in the posterior for the first lockdown to 17.5 mol s^{-1}, a reduction of 61%, surpassing the prior prediction of 44%. The second lockdown exhibits a reduction of around 40% compared to the 2019 prior for both the prior and posterior estimates. In the last lockdown, the decrease is less intense at 37% compared to the prior's 49%.

The lower panel of Fig. 5 shows the time series of prior and posterior NO_x lifetime estimates over Paris. Our Bayesian inversion framework captures seasonality, but the retrieved lifetime values should not be overinterpreted as chemically precise quantities. Our end-to-end test (Table 3 and Fig. 4) showed that the lifetime retrievals are subject to significant biases—up to 30%—highlighting the limitations of the method. This bias stems from the inherent asymmetry in the inversion sensitivity: the NO_2 line density is strongly and directly influenced by the strength of the NO_x emissions, whereas the lifetime exerts a more subtle control through the dampening of the increase in line densities with distance. In practice, the signal from NO_x emissions dominates the inversion, while the NO_x lifetime estimate is more a regularization parameter that prevents overfitting than a robust diagnostic of possible changes in atmospheric chemistry.

Figure 5 shows good agreement between prior and posterior lifetime estimates for most months, but in summertime the posterior lifetimes are often significantly below the prior values. This indicates that the NO_x emission reductions from 2018 to 2023 are not only supported by the satellite-observed changes in NO_2 column densities, but also require shorter effective lifetimes in the inversion to fit the observed spatial gradients. Taken together with the fact that posterior NO_x emissions are consistently lower than prior values, this points unambiguously to a substantial reduction in NO_x pollution over Paris. The simultaneous decrease in both posterior emissions and lifetimes, relative to the prior, reinforces the robustness of this conclusion: the observed NO_2 pattern cannot be reconciled without assuming cleaner conditions than those represented by the prior.

4.2.2 Seasonal and weekly cycle

In Winter, enhanced NO_x emissions are expected due to engine cold starts and increased residential heating demand (Paris generates the energy for heating within the city itself). Our analysis reveals a distinct seasonal cycle of NO_x emissions with a Winter:Summer ratio of 1.38 (Fig. 6a). Contrastingly, in the prior estimate, the fall months show the highest emissions (1.28 compared to the Summer). This could suggest that residential heating starts later than expected in the prior. We find that NO_x emissions are generally overestimated in the prior in Summer and underestimated in Winter. This is in line with the study of Lorente et al. (2019), who found that bottom-up emission inventories underestimate actual residential heating emissions in Winter months.

Additionally, a significant difference is found between NO_x emissions during low temperatures (<10°C) and high temperatures (>20°C) (Fig. 6b). We filtered the data ~~for weekdays, excluding~~ by excluding weekends, lockdown periods and the Summer holiday period (July-August) to mitigate potential holiday effects. The resulting average posterior difference between low and high-temperature emissions is 43-35 mol s^{-1}, a difference of 23%. This represents a similar but slightly stronger difference compared to the prior (43-33 mol s^{-1}).

We observe a distinct weekly cycle in Paris (Fig. 6c), starting with low emissions on Mondays, elevated levels on Thursdays and Fridays, and a reduction during the weekend (25%). This cycle is slightly more pronounced than initially assumed in the prior, which predicts a weekend reduction, calculated relative to the Mon-Fri average, of 22%. This weekend reduction is smaller than what was found by Lange et al. (2022) (40%) and Lorente et al. (2019) (35%). In Summer, the decrease in NO_x emissions in the weekend is much larger (39%) than in Winter (11%). This is likely because of a higher contribution of traffic emissions to the total emissions in the Summer months, whereas in Winter the share of traffic emissions may be smaller because of local residential heating and power generation. In Winter, the posterior weekend reduction is lower than in the prior inventory. This, again, ~~points~~ could point to a prior underestimation of residential heating~~or cold start emissions in the Winter months.~~. Additionally, the weaker weekly emission cycle observed in winter could be influenced by the effect of cold starts. On weekdays, vehicles are typically started early in the morning, while on weekends, car usage tends to begin later, closer to the TROPOMI overpass time. Weekend day emissions could then show up higher than without cold starts, dampening the weekly cycle.

4.2.3 Literature comparison

In Fig. 7, a comparison between prior and posterior emissions is presented alongside multiple inventory datasets. The interannual variation reveals a slight decrease in emissions in 2019, followed by a substantial decline in 2020 during the implementation of Covid-19 restrictions. Emissions veered back in 2021 and stabilized through 2023.

We compared our findings with other literature that estimates NO_x emissions in Paris (Fig. 7). Lorente et al. (2019) reported higher NO_x emissions for 2018, but only investigated these between January and June, while our estimation started from May 2018 onwards. We incorporated a corrected reaction rate constant for the oxidation of NO_2, which could contribute to the divergence in estimates. Lange et al. (2022) also estimated NO_x emissions for Paris from 2018 to 2020, reporting an average emission of 56.2 mol s^{-1}. Discrepancies here may arise from a different estimation method or variations in the definition of the Paris city area. Our emission levels align more closely with those reported by Lonsdale and Sun (2023). Their findings, presented in nmol m^{-2} s^{-1}, were converted to match our surface area unit. They observed lower values for 2019, comparable to our study for 2020 and 2021, and slightly lower values for 2022. The use of a fixed NO_x/NO_2 ratio of 1.32 could contribute to their slightly lower emissions.

We also compare our results to the CAMS-REGv7 inventory and NO_x emission estimates from AirParif, the air quality observatory in the Île-de-France region (AirParif, 2021, 2023). AirParif provides emission estimates averaged across the entire Île-de-France area, which we scaled to align with our Paris study domain. Given that NO_x emissions are higher closer to the city center and lower in outlying areas, we applied a scaling factor of 1.7 based on the ratio of emissions from the CAMS-

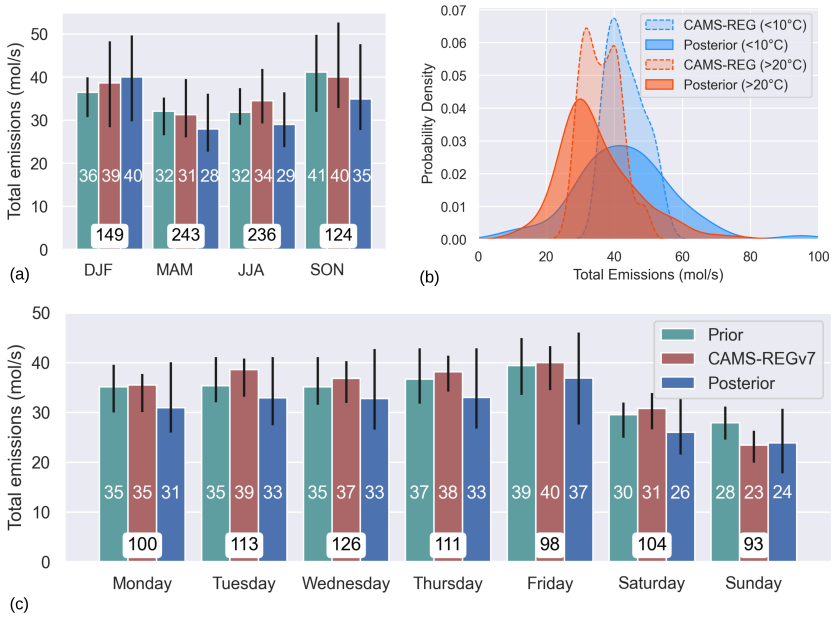

Figure 6. The seasonal (a) and weekly cycle (c) of NO_x emissions in Paris, of the prior,the posterior, and the CAMS-REGv7 inventory. White boxes display the count within each category. (c) shows the CAMS-REGv7 and Posterior NO_x emissions, grouped by temperature (<10°C (n=56) and >20°C (n=189). The weekends, Summer holidays and COVID lockdowns are filtered out here.

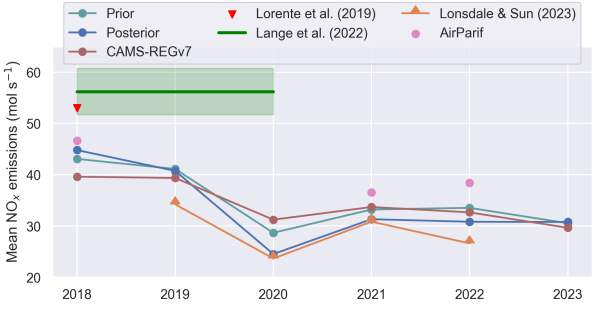

Figure 7. Annual NO_x emissions over the Paris from 2018 to 2023. For our study (blue) and other studies. Note that our analysis spans from May 2018 to July 2023, so the averages of 2018 and 2023 are not over the whole year.

REGv7 gridded inventory between the full Île-de-France region and our study area. These adjusted annual emission values are presented as pink dots in Fig. 7.

Since these values represent annual averages, they are not co-sampled with TROPOMI overpasses, which could explain the slightly higher NO_x emission estimates from AirParif compared to our estimates (blue line). For instance, TROPOMI

overpasses with sufficient cloud-free conditions are generally more frequent in Summer, which biases our annual averages toward this season, when NO_x emissions are typically lower.

5 Discussion and conclusion

We evaluated the performance of our superposition column model (Lorente et al., 2019) in estimating NO_x emissions within urban areas using satellite observations. Our investigation analyzed the ability of the forward model to calculate NO_2 columns over cities, given its use of simplified temporally and spatially averaged NO_x emissions, wind speed, NO_x lifetime, and NO_x/NO_2 ratios. We performed a comparison to synthetic NO_2 observations generated with the high-resolution Large Eddy Simulation model MicroHH, which simulates atmospheric dynamics and chemistry over a hypothetical city of 30 km $\times$30 km in minute detail. MicroHH simulates substantial variability in NO_x lifetime (1-9 h) and NO_x/NO_2 ratio (1.2-1.7) over the city domain, but the absolute deviation between NO_2 line densities simulated with the superposition model and with MicroHH stayed within 7%. This indicates that the superposition model is effective in describing the evolution of column NO_2 with distance over a large city, given known average NO_x/NO_2 and OH concentrations, despite averaging variable chemical and meteorological parameters over the city domain.

Tests with inferring NO_x emissions from synthetic NO_2 line densities simulated by MicroHH using the superposition model showed that simply minimizing the least-squares using a look-up table approach, as was done before in Lorente et al. (2019) frequently resulted in overfitting, where the NO_x lifetime is overestimated and the NO_x emissions are underestimated or vice versa. We propose a more formal Bayesian approach of the inversion of the NO_x emissions, which not only considers the fit to the observations, but also incorporates prior information about NO_x emissions and lifetime, to keep the solution in check. Although the Bayesian approach exhibits slightly larger discrepancies between the modeled and observed line densities, it yields solutions closer to the a priori known MicroHH emissions. The Bayesian approach reproduces the known NO_x emissions to within 4%, whereas the least-squares minimization, which does not take into account uncertainties in the prior emissions, reproduces emissions to within 20%.

We applied Bayesian inversion to infer a 5-year time series of daily NO_x emissions for Paris using TROPOMI NO_2 V2.4.0 retrievals from June 2018 to August 2023 under clear skies. Incorporating prior emission estimates from the TNO-MACC-III inventory, corrected for France's emission decrease reported by the European Environmental Agency, we found average NO_x emissions of 32 mol s^{-1}, which is 9% lower than the prior estimate. We observe an overall reduction in NO_x emissions between 2018 and 2023 of ~~18~~27%, compared to a reduction of 12% between 2018 and 2023 in the prior estimate. COVID-19 lockdowns led to sharp reductions of 61%, 40%, and 37% during the first, second, and third lockdown relative to emissions in the same period of the year before the COVID-19 measures. We observed a Winter:Summer emission ratio of 1.38, and significantly higher NO_x emissions on days with lower temperatures in Paris. We find a weekend NO_x reduction of 25%, slightly more pronounced than the weekend effect of 22% in the emission inventory. We demonstrated that the improved Bayesian inversion method of the superposition model offers a reliable and efficient means to monitor daily NO_x emissions and evaluate policies in urban areas.

Code and data availability. The TROPOMI L2 product used in this study is available through the TEMIS portal (https://www.temis.nl/airpollution/no2col/no2_euro_tropomi_cams.php, last access: 6 January 2025). CAMS model data were retrieved from the CAMS Atmosphere Data Store (https://ads.atmosphere.copernicus.eu, last access: 6 January 2026) and its predecessor hosted by Météo-France. The MicroHH code used for the calculations is available from GitHub (https://github.com/microhh/microhh, branch main_kpp, last access: 6 January 2025). The inventory from TNO (TNO-MACC-III) is available on request by contacting HDG. Access to the CAMS-REG-v7 is provided through the Emissions of atmospheric Compounds of Ancillary Data (ECCAD) system. Since the ECCAD system requires a registration and login, a sample of the emission files has been made available for download directly. This sample includes data for the year 2017 and is available through https://eccad.aeris-data.fr/essd-surf-emis-cams-reg/ (last access: 6 January 2025). Daily NO_x emission estimates will be made available through zenodo (Mols, 2025).

Author contributions. AM and KFB designed the study. AM performed the data analysis with support from KFB. AM wrote the manuscript with contributions from KFB, MK and HDG. MK performed the simulations in MicroHH. HDG provided the bottom-up inventory and guidance on the interpretation thereof

Competing interests. The authors declare that they have no conflict of interest.

References

AirParif: Émissions de polluants atmospériques et de gaz à effet de serre, Tech. rep., 2021.

AirParif: Émissions et consommations 2021 en Île-de-France (estimations faites en 2023), 2023.

Beirle, S., Boersma, K. F., Platt, U., Lawrence, M. G., and Wagner, T.: Megacity emissions and lifetimes of nitrogen oxides probed from space, Science, 333, 1737–1739, 2011.

Bernard, Y., Miller, J., Wappelhorst, S., and Braun, C.: Impacts of the Paris low-emission zone and implications for other cities, TRUE–The Real Urban Emissions Initiative, United Kingdom, ISBN, 1744072, 2020.

Boningari, T. and Smirniotis, P. G.: Impact of nitrogen oxides on the environment and human health: Mn-based materials for the NOx abatement, Current Opinion in Chemical Engineering, 13, 133–141, 2016.

Brioude, J., Angevine, W. M., Ahmadov, R., Kim, S.-W., Evan, S., McKeen, S. A., Hsie, E.-Y., Frost, G. J., Neuman, J. A., and Pollack, I. B.: Top-down estimate of surface flux in the Los Angeles Basin using a mesoscale inverse modeling technique: assessing anthropogenic emissions of CO, NO x and CO 2 and their impacts, Atmospheric Chemistry and Physics, 13, 3661–3677, 2013.

Burkholder, J. B., Sander, S. P., Abbatt, J. P. D., Barker, J. R., Cappa, C., Crounse, J. D., Dibble, T. S., Huie, R. E., Kolb, C. E., and Kurylo, M. J.: Chemical kinetics and photochemical data for use in atmospheric studies; evaluation number 19, Tech. rep., 2020.

Cheng, X., Hao, Z., Zang, Z., Liu, Z., Xu, X., Wang, S., Liu, Y., Hu, Y., and Ma, X.: A new inverse modeling approach for emission sources based on the DDM-3D and 3DVAR techniques: an application to air quality forecasts in the Beijing–Tianjin–Hebei region, Atmospheric Chemistry and Physics, 21, 13 747–13 761, 2021.

de Foy, B. and Schauer, J. J.: An improved understanding of NOx emissions in South Asian megacities using TROPOMI NO2 retrievals, Environmental Research Letters, 17, 024 006, 2022.

de Foy, B., Wilkins, J. L., Lu, Z., Streets, D. G., and Duncan, B. N.: Model evaluation of methods for estimating surface emissions and chemical lifetimes from satellite data, Atmospheric Environment, 98, 66–77, 2014.

Denier van der Gon, H., Hendriks, C., Kuenen, J., Segers, A., and Visschedijk, A.: TNO Report: Description of current temporal emission patterns and sensitivity of predicted AQ for temporal emission patterns, Tech. rep., TNO, Utrecht, 2011.

Douros, J., Eskes, H., van Geffen, J., Boersma, K. F., Compernolle, S., Pinardi, G., Blechschmidt, A.-M., Peuch, V.-H., Colette, A., and Veefkind, P.: Comparing Sentinel-5P TROPOMI NO 2 column observations with the CAMS-regional air quality ensemble, EGUsphere, pp. 1–40, 2022.

EEA: Air quality in Europe 2019, 2019.

EEA: Air quality in Europe 2022, 2022.

EEA: France – air pollution country fact sheet, 2023.

Erisman, J. W. and Draaijers, G. P. J.: Atmospheric deposition: in relation to acidification and eutrophication, Elsevier, 1995.

Eskes, H. J. and Boersma, K. F.: Averaging kernels for DOAS total-column satellite retrievals, Atmospheric Chemistry and Physics, 3, 1285–1291, 2003.

EU: Air quality: traffic measures could effectively reduce NO2 concentrations by 40% in Europe's cities, 2019.

Fischer, E. V., Jacob, D. J., Yantosca, R. M., Sulprizio, M. P., Millet, D. B., Mao, J., Paulot, F., Singh, H. B., Roiger, A., and Ries, L.: Atmospheric peroxyacetyl nitrate (PAN): a global budget and source attribution, Atmospheric Chemistry and Physics, 14, 2679–2698, 2014.

Goldberg, D. L., Harkey, M., de Foy, B., Judd, L., Johnson, J., Yarwood, G., and Holloway, T.: Evaluating NO x emissions and their effect on O 3 production in Texas using TROPOMI NO 2 and HCHO, Atmospheric Chemistry and Physics, 22, 10 875–10 900, 2022.

Guevara, M., Jorba, O., Tena, C., Denier van der Gon, H., Kuenen, J., Elguindi-Solmon, N., Darras, S., Granier, C., and Pérez García-Pando, C.: CAMS-TEMPO: global and European emission temporal profile maps for atmospheric chemistry modelling, Earth System Science Data Discussions, 2020, 1–60, 2020.

Guevara, M., Jorba, O., Soret, A., Petetin, H., Bowdalo, D., Serradell, K., Tena, C., Denier van der Gon, H., Kuenen, J., and Peuch, V.-H.: Time-resolved emission reductions for atmospheric chemistry modelling in Europe during the COVID-19 lockdowns, Atmospheric Chemistry and Physics, 21, 773–797, 2021.

Hakkarainen, J., Kuhlmann, G., Koene, E., Santaren, D., Meier, S., Krol, M. C., van Stratum, B. J. H., Ialongo, I., Chevallier, F., and Tamminen, J.: Analyzing nitrogen dioxide to nitrogen oxide scaling factors for data-driven satellite-based emission estimation methods: A case study of Matimba/Medupi power stations in South Africa, Atmospheric Pollution Research, 15, 102 171, 2024.

Ikhlasse, H., Benjamin, D., Vincent, C., and Hicham, M.: Environmental impacts of pre/during and post-lockdown periods on prominent air pollutants in France, Environment, Development and Sustainability, 23, 14 140–14 161, 2021.

Jacob, D.: Introduction to Atmospheric Chemistry, Princeton University Press, 1999.

Johnson, M. S., Philip, S., Meech, S., Kumar, R., Sorek-Hamer, M., Shiga, Y. P., and Jung, J.: Insights into the long-term (2005–2021) spatiotemporal evolution of summer ozone production sensitivity in the Northern Hemisphere derived with the Ozone Monitoring Instrument (OMI), Atmospheric Chemistry and Physics, 24, 10 363–10 384, 2024.

Krol, M., van Stratum, B., Anglou, I., and Boersma, K. F.: Evaluating NO x stack plume emissions using a high-resolution atmospheric chemistry model and satellite-derived NO 2 columns, Atmospheric Chemistry and Physics, 24, 8243–8262, 2024.

Kuenen, J., Dellaert, S., Visschedijk, A., Jalkanen, J.-P., Super, I., and Denier van der Gon, H.: CAMS-REG-v4: a state-of-the-art high-resolution European emission inventory for air quality modelling, Earth System Science Data, 14, 491–515, 2022.

Kuenen, J. J. P., Visschedijk, A. J. H., Jozwicka, M., and Denier Van Der Gon, H. A. C.: TNO-MACC_II emission inventory; a multi-year (2003–2009) consistent high-resolution European emission inventory for air quality modelling, Atmospheric Chemistry and Physics, 14, 10 963–10 976, 2014.

Kurokawa, J.-i., Yumimoto, K., Uno, I., and Ohara, T.: Adjoint inverse modeling of NOx emissions over eastern China using satellite observations of NO2 vertical column densities, Atmospheric Environment, 43, 1878–1887, 2009.

Lange, K., Richter, A., and Burrows, J. P.: Variability of nitrogen oxide emission fluxes and lifetimes estimated from Sentinel-5P TROPOMI observations, Atmospheric Chemistry and Physics, 22, 2745–2767, 2022.

Lange, K., Richter, A., Bösch, T., Zilker, B., Latsch, M., Behrens, L. K., Okafor, C. M., Bösch, H., Burrows, J. P., and Merlaud, A.: Validation of GEMS tropospheric NO2 columns and their diurnal variation with ground-based DOAS measurements, Atmospheric Measurement Techniques, 17, 6315–6344, 2024.

Liu, F., Tao, Z., Beirle, S., Joiner, J., Yoshida, Y., Smith, S. J., Knowland, K. E., and Wagner, T.: A new method for inferring city emissions and lifetimes of nitrogen oxides from high-resolution nitrogen dioxide observations: a model study, Atmospheric Chemistry and Physics, 22, 1333–1349, 2022.

Lonsdale, C. R. and Sun, K.: Nitrogen oxides emissions from selected cities in North America, Europe, and East Asia observed by the TROPOspheric Monitoring Instrument (TROPOMI) before and after the COVID-19 pandemic, Atmospheric Chemistry and Physics, 23, 8727–8748, 2023.

Lorente, A., Boersma, K. F., Eskes, H. J., Veefkind, J. P., Van Geffen, J., De Zeeuw, M. B., Denier Van Der Gon, H. A. C., Beirle, S., and Krol, M. C.: Quantification of nitrogen oxides emissions from build-up of pollution over Paris with TROPOMI, Scientific reports, 9, 1–10, 2019.

Meier, S., Koene, E. F. M., Krol, M., Brunner, D., Damm, A., and Kuhlmann, G.: A lightweight NO 2-to-NO x conversion model for quantifying NO x emissions of point sources from NO 2 satellite observations, Atmospheric Chemistry and Physics, 24, 7667–7686, 2024.

Pazmiño, A., Beekmann, M., Goutail, F., Ionov, D., Bazureau, A., Nunes-Pinharanda, M., Hauchecorne, A., and Godin-Beekmann, S.: Impact of the COVID-19 pandemic related to lockdown measures on tropospheric NO 2 columns over Île-de-France, Atmospheric Chemistry and Physics, 21, 18 303–18 317, 2021.

Ražnjević, A., Van Heerwaarden, C., Van Stratum, B., Hensen, A., Velzeboer, I., Van Den Bulk, P., and Krol, M.: Interpretation of field observations of point-source methane plume using observation-driven large-eddy simulations, Atmospheric Chemistry and Physics, 22, 6489–6505, 2022.

Rey-Pommier, A., Chevallier, F., Ciais, P., Broquet, G., Christoudias, T., Kushta, J., Hauglustaine, D., and Sciare, J.: Quantifying NO x emissions in Egypt using TROPOMI observations, Atmospheric Chemistry and Physics Discussions, 2022, 1–21, 2022.

Riess, T. C. V. W., Boersma, K. F., Van Roy, W., de Laat, J., Dammers, E., and van Vliet, J.: To new heights by flying low: Comparison of aircraft vertical NO 2 profiles to model simulations and implications for TROPOMI NO 2 retrievals, EGUsphere, 2023, 1–25, 2023.

Rijsdijk, P., Eskes, H., Dingemans, A., Boersma, F., Sekiya, T., Miyazaki, K., and Houweling, S.: Quantifying uncertainties of satellite NO 2 superobservations for data assimilation and model evaluation, EGUsphere, 2024, 1–42, 2024.

Rijsdijk, P., Eskes, H., Dingemans, A., Boersma, K. F., Sekiya, T., Miyazaki, K., and Houweling, S.: Quantifying uncertainties in satellite NO2 superobservations for data assimilation and model evaluation, Geoscientific Model Development, 18, 483–509, 2025.

Seinfeld, J. H. and Pandis, S. N.: Atmospheric chemistry and physics: from air pollution to climate change, John Wiley & Sons, 2016.

Sierk, B., Fernandez, V., Bézy, J.-L., Meijer, Y., Durand, Y., Courrèges-Lacoste, G. B., Pachot, C., Löscher, A., Nett, H., and Minoglou, K.: The Copernicus CO2M mission for monitoring anthropogenic carbon dioxide emissions from space, in: International Conference on Space Optics—ICSO 2020, vol. 11852, pp. 1563–1580, SPIE, 2021.

Stavrakou, T., Müller, J.-F., Boersma, K. F., Van Der A, R. J., Kurokawa, J., Ohara, T., and Zhang, Q.: Key chemical NO x sink uncertainties and how they influence top-down emissions of nitrogen oxides, Atmospheric Chemistry and Physics, 13, 9057–9082, 2013.

Tilstra, L. G., de Graaf, M., Trees, V., Litvinov, P., Dubovik, O., and Stammes, P.: A directional surface reflectance climatology determined from TROPOMI observations, Atmospheric Measurement Techniques Discussions, 2023, 1–29, 2023.

Tu, R., Xu, J., Wang, A., Zhai, Z., and Hatzopoulou, M.: Effects of ambient temperature and cold starts on excess NOx emissions in a gasoline direct injection vehicle, Science of the Total Environment, 760, 143 402, 2021.

Valin, L. C., Russell, A. R., and Cohen, R. C.: Variations of OH radical in an urban plume inferred from NO2 column measurements, Geophysical Research Letters, 40, 1856–1860, 2013.

van Geffen, J., Eskes, H., Boersma, K., and Veefkind, J.: TROPOMI ATBD of the total and tropospheric NO2 data products: S5P-KNMI-L2-0005-RP, Tech. rep., 2022.

Van Geffen, J., Eskes, H., Compernolle, S., Pinardi, G., Verhoelst, T., Lambert, J.-C., Sneep, M., Ter Linden, M., Ludewig, A., and Boersma, K. F.: Sentinel-5P TROPOMI NO 2 retrieval: impact of version v2. 2 improvements and comparisons with OMI and ground-based data, Atmospheric Measurement Techniques, 15, 2037–2060, 2022.

Van Heerwaarden, C. C., Van Stratum, B. J. H., Heus, T., Gibbs, J. A., Fedorovich, E., and Mellado, J. P.: MicroHH 1.0: A computational fluid dynamics code for direct numerical simulation and large-eddy simulation of atmospheric boundary layer flows, Geoscientific Model Development, 10, 3145–3165, 2017.

Vilà-Guerau de Arellano, J., Dosio, A., Vinuesa, J.-F., Holtslag, A. A. M., and Galmarini, S.: The dispersion of chemically reactive species in the atmospheric boundary layer, Meteorology and Atmospheric Physics, 87, 23–38, 2004.

Visser, A. J., Boersma, K. F., Ganzeveld, L. N., and Krol, M. C.: European NO x emissions in WRF-Chem derived from OMI: impacts on summertime surface ozone, Atmospheric Chemistry and Physics, 19, 11 821–11 841, 2019.

Vitousek, P. M., Aber, J. D., Howarth, R. W., Likens, G. E., Matson, P. A., Schindler, D. W., Schlesinger, W. H., and Tilman, D. G.: Human alteration of the global nitrogen cycle: sources and consequences, Ecological applications, 7, 737–750, 1997.

WHO: WHO global air quality guidelines: particulate matter (PM2. 5 and PM10), ozone, nitrogen dioxide, sulfur dioxide and carbon monoxide, World Health Organization, 2021.

Yan, C., Nie, W., Vogel, A. L., Dada, L., Lehtipalo, K., Stolzenburg, D., Wagner, R., Rissanen, M. P., Xiao, M., and Ahonen, L.: Size-dependent influence of NOx on the growth rates of organic aerosol particles, Science advances, 6, eaay4945, 2020.

Zhang, Q., Boersma, K. F., Zhao, B., Eskes, H., Chen, C., Zheng, H., and Zhang, X.: Quantifying daily NO x and CO 2 emissions from Wuhan using satellite observations from TROPOMI and OCO-2, Atmospheric Chemistry and Physics Discussions, pp. 1–18, 2022.

Zhu, Q., Laughner, J. L., and Cohen, R. C.: Estimate of OH trends over one decade in North American cities, Proceedings of the National Academy of Sciences, 119, e2117399 119, 2022.